Electrical power management and optimization with nonlinear energy harvesting structures

Wen Cai and Ryan L Harne [iD]

Abstract

In recent years, great advances in understanding the opportunities for nonlinear vibration energy harvesting systems have been achieved giving attention to either the structural or electrical subsystems. Yet, a notable disconnect appears in the knowledge on optimal means to integrate nonlinear energy harvesting structures with effective nonlinear rectifying and power management circuits for practical applications. Motivated to fill this knowledge gap, this research employs impedance principles to investigate power optimization strategies for a nonlinear vibration energy harvester interfaced with a bridge rectifier and a buck-boost converter. The frequency and amplitude dependence of the internal impedance of the harvester structure challenges the conventional impedance matching concepts. Instead, a system-level optimization strategy is established and validated through simulations and experiments. Through careful studies, the means to optimize the electrical power with partial information of the electrical load is revealed and verified in comparison to the full analysis. These results suggest that future study and implementation of optimal nonlinear energy harvesting systems may find effective guidance through power flow concepts built on linear theories despite the presence of nonlinearities in structures and circuits.

Introduction

The possibilities for wireless, self-sufficient electrical supplies to advance myriad applications in an emerging "Internet of things" are recently well established (Beeby et al., 2006; Mitcheson et al., 2008). For instance, self-sufficient power resources would propel new and future practices of structural health and condition monitoring, wildlife tracking, and precision agriculture (Beeby et al., 2006; Jawad et al., 2017; Shafer et al., 2015). In addition, achievements in energy-efficient circuit design (Chandrakasan et al., 1998; Davis et al., 2002) suggest that the possibilities for a transformative "energy harvesting" infrastructure are closer at hand than ever.

Among all kinds of ambient energy sources, vibrational energy is a desirable choice to harvest for the abundance and persistence of kinetic energy in applications. Because many energy harvesting devices are composed from structural oscillator designs, the narrow frequency of resonance for linear harvester systems is unfavorable for robustness in electrical power delivery. As a result, a wide variety of methods have been introduced to increase the frequency range of effective energy capture in vibration energy harvesters. For

example, self-tuning (Roundy and Zhang, 2005), harvester arrays (Xiao et al., 2014), mechanical stoppers (Wu et al., 2014), nonlinearity (Gu and Livermore, 2011; Harne and Wang, 2013; Sebald et al., 2011), and other concepts have been investigated. Bistable nonlinearities have attracted broad attention due to the non-resonant nature of oscillation that is less susceptible to performance deterioration in low-level vibration environments (Erturk et al., 2009; Ferrari et al., 2010; Harne et al., 2013; Scarselli et al., 2016). A bistable oscillator has two statically stable equilibria, which makes it possible to exhibit three classes of vibration in consequence to single-frequency excitation: snap-through, quasi-linear, and chaotic vibration (Harne and Wang, 2013). The non-resonant nature of snap-through enables it to

Department of Mechanical and Aerospace Engineering, The Ohio State University, Columbus, OH, USA

Corresponding author:
Ryan L Harne, Department of Mechanical and Aerospace Engineering, The Ohio State University, 201 W. 19th Avenue, Columbus, OH 43210, USA.
Email: harne.3@osu.edu

be triggered in a diverse range of excitation environments, especially at low frequencies characteristic of practical ambient vibrations (Cottone et al., 2009). In addition, snap-through may yield large velocities of harvester motion that corresponds to high output power. For example, Erturk et al. (2009) demonstrated a 200% increase in the open-circuit voltage amplitude with harmonic excitation by leveraging snap-through vibrations of a bistable energy harvester, while Ferrari et al. (2010) found an 80% increase in the root mean square (RMS) voltage with white noise excitation.

Since microelectronic devices require a regulated direct current (DC) input voltage, a rectifying circuit is necessary for energy harvesters to convert the oscillating alternating current (AC) signals to DC power. There are two classes of rectification: passive and active rectification (Szarka et al., 2012). Comparing with the passive methods, active methods may improve the power conversion efficiency at low power levels (Le et al., 2006). On the other hand, active rectification may require careful design to overcome challenges such as "cold start" (Lam et al., 2006). Therefore, despite the possible improvements from active rectification methods, passive rectification such as full-wave diode bridges are widely employed for rectification needs in vibration energy harvesting investigations. To improve power capture, such rectifiers may be modified via switching strategies. For instance, the parallel synchronized switching harvesting on inductor (SSHI) presented by Guyomar et al. (2005) adds an inductor and a switch in parallel with the linear piezoelectric element electrodes to the input of the rectifier bridge so as to enhance power potentially by 900% according to the switch-controlled current flow (Guyomar et al., 2005). Other types of nonlinear circuit like series-SSHI and optimized series-SSHI may improve the output power as well (Garbuio et al., 2009; Lefeuvre et al., 2006; Makihara et al., 2006).

Yet, for a selected circuit, the optimal output power is only achieved when the load impedance matches the source impedance. Liang and Liao (2012) characterized such influences for a linear piezoelectric energy harvester to reveal optimal working condition for a variety of nonlinear rectification circuits (Liang and Liao, 2012). On the other hand, rectified voltages from piezoelectric energy harvesters may significantly exceed the required operational voltages of rechargeable batteries and microelectronics. As such, a DC–DC converter is introduced after the piezoelectric voltage rectification stage to provide the needed power management (Ottman et al., 2002). Lefeuvre et al. (2007) present the roles of a buck-boost converter working in the discontinuous current mode (DCM), revealing that the nonlinear converter appears as a resistive load impedance with respect to the linear piezoelectric energy harvester platform regardless of the real load resistance bearing the DC power. These findings demonstrate that the

nonlinear rectification and power management are crucial to understand in order to effectively implement linear piezoelectric energy harvesters in the conventional resonant vibration mode.
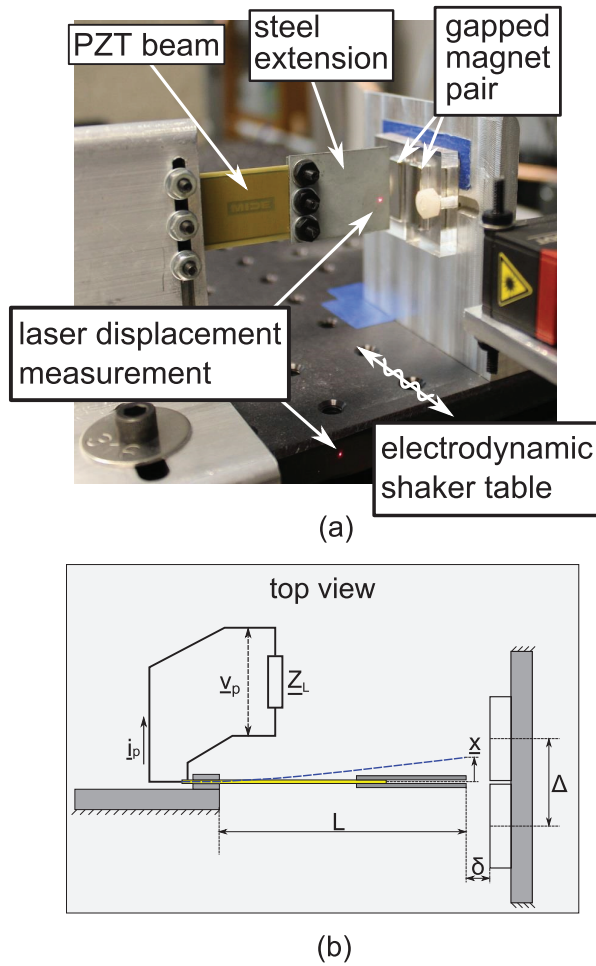
Considering the state of the art, nonlinearities in the vibration energy harvesting structure or nonlinearities in the rectification and power management stages may be leveraged for effective DC power delivery. On the other hand, understanding of the suitable integration of these subsystems is lacking so that a disconnect of knowledge exists on the system-level harvester implementation. In order to bridge the gap in the understanding of optimal use of nonlinear energy harvesters with nonlinear rectification and power management circuits, this research takes a first step forward to study the structural–electrical interactions manifest in a nonlinear energy harvester coupled with a passive diode bridge rectifier and a buck-boost DC–DC converter. By harnessing the principles of impedance, new insights are revealed on practical strategies for system optimization.

This report is organized as follows. The next section studies the internal impedance of the nonlinear harvester structural platform. Then, rectification and buck-boost converter stages are taken into detailed consideration. Following validation efforts, the impedance changes observed at the system level are revealed and the optimal working conditions for a buck-boost DC–DC converter integrated with the nonlinear harvester are uncovered through a rigorous impedance-based analysis. Finally, a summary of key insights from this work concludes the report.

Source/load modeling of nonlinear energy harvesting system

Energy harvester platform

The structural platform of the experimental energy harvesting system considered in this work is shown in Figure 1(a). A piezoelectric cantilever (PPA-2014; Mide Technology) has the clamped end affixed to an electrodynamic shaker (APS Dynamics 400). The shaker is driven by a controller (Vibration Research Controller VR9500) and amplifier (Crown XLS 2500). Laser displacement sensors (Micro-Epsilon ILD-1420) are used to measure the absolute displacements of the beam tip and shaker table. An accelerometer (PCB Piezotronics 333B40) is used to provide feedback for the shaker controller. The nonlinearity exploited in this research is a bistability realized by magnetoelastic effects. Specifically, at the free end of the piezoelectric cantilever a steel extension is added to decrease the lowest order natural frequency of the beam and introduce nonlinearity by magnetic forces from an adjacent pair of neodymium magnets. The total mass of the extension is 9 g. The length L of the cantilever beam and steel extension is 60.8 mm. With careful adjustment of the
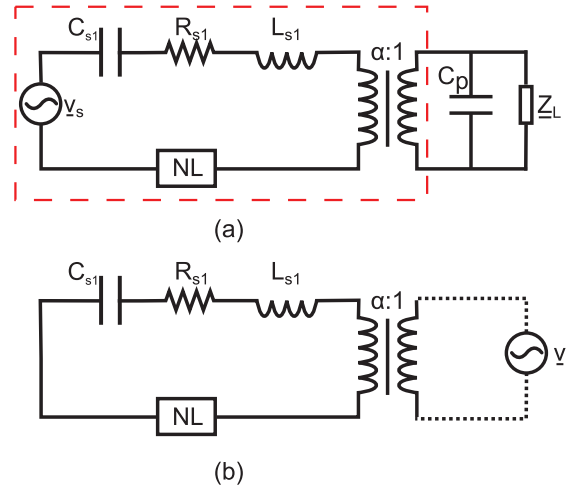
Figure 1. (a) Photograph and (b) schematic of the experimental setup.

Figure 2. (a) Equivalent circuit of a base-excited nonlinear energy harvesting system and (b) equivalent circuit for the internal source impedance determination.

distances δ and Δ shown in Figure 1(b), the bistable nonlinearity is realized (Erturk and Inman, 2011; Feeny et al., 2001; Hikihara and Kawagoshi, 1996; Moon and Holmes, 1979). Based on the survey of state-of-the-art developments in section "Introduction," the advancements provided by a bistable vibration energy harvester are associated with the snap-through behavior. Therefore, in the following investigations the study places attention on scrutinizing the DC power delivery from the snap-through response.

Governing equations of motion for the energy harvesting system

In this work, the frequencies of base acceleration are around the lowest order linear natural frequency of the piezoelectric cantilever, so that the deflection of the cantilever is primarily in the first vibration mode (Erturk and Inman, 2008). Therefore, a single-degree-of-freedom model is adopted to study the nonlinear energy harvesting system. The governing equations are expressed as

$$m\ddot{\underline{x}} + d\dot{\underline{x}} + k_1(1-p)\underline{x} + k_3\underline{x}^3 + \alpha\underline{v}_p = -m\ddot{\underline{z}} \quad (1a)$$

$$C_p\dot{\underline{v}}_p + \underline{i}_p = \alpha\dot{\underline{x}} \quad (1b)$$

where $\underline{x}$ is the beam tip displacement relative to the motion of the base displacement $\underline{z}$; m, d, k_1, and k_3 are the equivalent lumped mass, viscous damping, linear stiffness, and nonlinear stiffness corresponding to the first vibration mode, respectively; p is the load parameter, which is used to indicate the influence of magnetic forces on reducing the linear stiffness; α is the electromechanical coupling constant; C_p is the internal capacitance of the piezoelectric beam; $\underline{v}_p$ is the voltage across the piezoelectric beam electrodes; and $\underline{i}_p$ is the corresponding current that passes into the harvesting circuit impedance $\underline{Z}_L$ as exemplified in Figure 1(b). The overdot operator indicates differentiation with respect to time t.

Studies have shown the analogy between mechanical and electrical systems in the energy harvesting literature (Kong et al., 2010; Liang and Liao, 2012; Yang and Tang, 2009). Here, such concept is employed to identify an equivalent electrical system shown in Figure 2(a) that represents the vibration energy harvesting system. The electromechanical coupling constant α is interpreted as a transformer turn ratio. In Figure 2(a), $\underline{v}_{s1}$ corresponds to the base acceleration via $\underline{v}_{s1} = -m\ddot{\underline{z}}$. The inductance L_{s1}, resistance R_{s1}, and capacitance C_{s1} in the circuit, respectively, relate to the mass $L_{s1} = m$, viscous damping $R_{s1} = d$, and compliance $C_{s1} = 1/k_1$. For the nonlinearity in the energy harvesting system characterized by the negative linear stiffness $-pk_1$ and

Table 1. Experimentally identified system parameters.

m (g)	d (N s/m)	k_1 (N/m)	p (dim)
9.45	0.194	722	1.27

k_3 (MN/m^3)	C_p (nF)	α (mN/V)	
86	88	1.4	

nonlinear stiffness k_3, a general impedance *NL* block is shown in Figure 2(b) that will be clearly defined in the subsequent modeling of this work. In the following study, the components in the red dashed box are collectively considered to be the source impedance $\underline{Z}_s$ of the nonlinear energy harvesting system. The current through this source impedance is related to the relative velocity of the beam tip via $\underline{i} = \alpha \underline{\dot{x}}$.

Experimental system identification

To identify the parameters of the nonlinear cantilever, an impulsive ring-down test is first conducted to ensure the symmetry of the two static equilibria via identical linear natural frequencies of oscillation around each stable equilibrium. The equivalent lumped mass m and the linear stiffness k_1 are calculated by classical relations (Erturk and Inman, 2011). After determining the natural frequency ω_n from the ring-down experiments and measuring the static equilibria x^*, the load parameter p and nonlinear stiffness k_3 are found by

$$p = 1 + \frac{\omega_n^2 m}{2k_1}, \ k_3 = \frac{k_1(p-1)}{(x^*)^2} \qquad (2)$$

The identified parameters of the nonlinear energy harvester platform are shown in Table 1.

Source impedance characterization

The original source $\underline{v}_{s1}$ in Figure 2(a) is removed to study the source impedance $\underline{Z}_s$ of the harvester itself. Instead, an AC voltage $\underline{v}$ is connected to the output terminal, which is referred to as the driven voltage shown in Figure 2(b). Then, the governing equation is

$$m\underline{\ddot{x}} + d\underline{\dot{x}} + k_1(1-p)\underline{x} + k_3\underline{x}^3 = \alpha\underline{v} \qquad (3)$$

The driven voltage is

$$\underline{v} = -\underline{V}\cos(\underline{\omega}t) \qquad (4)$$

The governing equation (3) after non-dimensionalization is

$$x'' + \eta x' + (1-p)x + \beta x^3 = \kappa v \qquad (5)$$

The corresponding non-dimensional parameters are defined as follows

$$x = \frac{x}{x_0}, \ V = \frac{V}{V_0}, \ \tau = \omega_0 t$$

$$\beta = \frac{k_3 x_0^2}{k_1}, \ \kappa = \frac{\alpha V_0}{k_1 x_0} \qquad (6)$$

$$\omega_0 = \sqrt{\frac{k_1}{m}}, \ \omega = \frac{\omega}{\omega_0}, \ \eta = \frac{d}{m\omega_0}$$

where x_0 and V_0 are the characteristic length and voltage, respectively, that are defined to be 1 mm and 1 V, respectively. These selections are made to keep the non-dimensional response values around the order of 1.

Using the principles of harmonic balance (Harne and Wang, 2017), the solution to equation (5) may be approximated as

$$x(\tau) = c(\tau) + a(\tau)\sin(\omega\tau) + b(\tau)\cos(\omega\tau) \qquad (7)$$

The coefficients of the constant, sine, and cosine terms are collected after substituting equation (7) into equation (5). Since only the fundamental frequency of vibration is considered in equation (7), the higher order harmonics are neglected. In addition, the coefficients are assumed to vary slowly in non-dimensional time. The resulting system of equations collecting together constant and sinusoidal terms is

$$-\eta c' = c\left(1 - p + \frac{3}{2}\beta r^2 + \beta c^2\right) \qquad (8a)$$

$$-\eta a' + 2\omega b' = a\Lambda - bX \qquad (8b)$$

$$-2\omega a' - \eta b' = aX + b\Lambda + V\kappa \qquad (8c)$$

The following terms are identified

$$r^2 = a^2 + b^2, \ \Lambda = 1 - p - \omega^2 + \frac{3}{4}\beta r^2 + 3\beta c^2, \ X = \eta\omega \qquad (9)$$

The steady-state behavior of the nonlinear equivalent source is determined by first solving equation (8a) to yield

$$c = 0 \text{ or } c^2 = \frac{p-1}{\beta} - \frac{3}{2}r^2 \qquad (10)$$

Here, the snap-through behavior is related to $c = 0$ so that the displacements of the piezoelectric cantilever undergo zero-mean oscillations. Therefore, only $c = 0$ is considered in the following evaluations.

Then, combining equations (8b) and (8c), the snap-through response is studied through solutions to the roots of the polynomial (equation (11))

$$(\Lambda^2 + X^2)r^2 = (V\kappa)^2 \qquad (11)$$
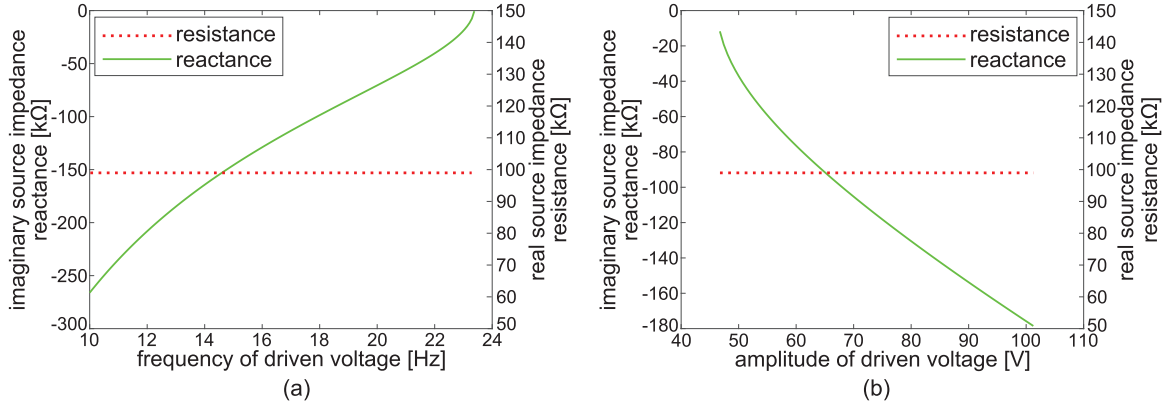
Figure 3. (a) Driven voltage frequency and (b) amplitude influences on the source impedance.

Equation (11) is a cubic polynomial in terms of r^2. Complex and negative solutions are not physically meaningful. Stability of the roots is assessed according to the eigenvalues of the associated Jacobian from equation (8) (Harne and Wang, 2017).

For the circuit shown in Figure 2(b), the voltage and current are expressed in a complex exponential notation to characterize the source impedance $\underline{Z}_s$

$$\underline{Z}_s = \frac{\underline{v}}{\underline{i}} = \frac{-\underline{V}e^{j\omega t}}{\alpha \underline{\dot{x}}} = \frac{-V_0}{\alpha x_0 \omega_0} \frac{Ve^{j\omega\tau}}{\omega r \cdot e^{j(\omega\tau - \varphi_i)}} = \frac{-V_0 V e^{\varphi_i}}{\alpha x_0 \omega_0 \omega r} \tag{12}$$

where

$$\tan \varphi_i = \frac{-b}{a} \tag{13}$$

Figure 3 presents the source impedance results that characterize the impedance change for a change in the driven voltage. The experimentally identified system parameters from Table 1 are used to generate Figure 3 using the aforementioned model. The fixed amplitude of the driven voltage for Figure 3(a) is 51 V and the fixed driven voltage frequency for Figure 3(b) is 22 Hz. Since attention is only on the snap-through behavior, the source impedance does not exist in the whole range of the driven voltage frequency and amplitude for Figure 3. In addition, it is observed that the reactance is frequency and amplitude dependent. Such dependencies are evidence of the cubic nonlinearity and the presence of negative linear stiffness via the bistable nonlinearity.

In the steady-state analysis, only the fundamental frequency vibration is considered. Therefore, a linearized version of the system (5) is

$$x'' + \eta x' + \left(1 - p + \frac{3\beta}{4}r^2\right)x = \kappa v \tag{14}$$
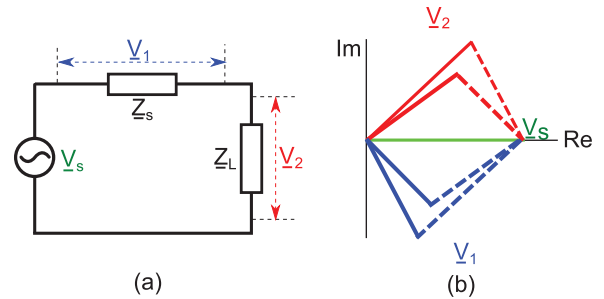
Figure 4. (a) The simplified circuit schematic for a nonlinear harvesting system and (b) voltage shown in the complex plane.

From equation (14), the roles that the nonlinear and negative stiffness terms play to culminate in the system behaviors become clear. The terms modeled as the generic *NL* impedance in Figure 2 are therefore analogous to a capacitor that has a response-dependent capacitance value. This also explains the amplitude-dependent source reactance in Figure 3. In contrast, the resistance in Figure 3 is independent of the frequency and amplitude of the driven voltage, due to the nature of the viscous damping–based resistance $R_{s1} = d$ in Figure 2.

For any harmonically driven electrical system, optimal power delivery to a load is achieved when the load impedance is the complex conjugate of the source impedance. A suboptimal approach is resistive impedance matching that may be relevant for vibration energy harvesting systems (Kong et al., 2010). Figure 4(a) shows a simplified circuit schematic for a vibration energy harvesting system. The source voltage amplitude is $\underline{V}_s$, characteristic of the base acceleration. The corresponding voltages across the source impedance and load impedance are, respectively, $\underline{V}_1$ and $\underline{V}_2$. Figure 4(b) presents these voltages in the complex plane. By Kirchhoff's law, the combination of $\underline{V}_1$ and $\underline{V}_2$ is equal

to $\underline{V}_s$. For the nonlinear system examined here, if the load impedance is changed to match the source impedance, the voltage across the load impedance is changed due to the amplitude-dependent nature of the system. This correspondingly changes $\underline{V}_1$. As a result, a standard practice of impedance matching is significantly challenged. Therefore, in this research, the investigation of optimal power delivery from the nonlinear energy harvesting system with power management circuitry requires studious consideration of the platform–circuit system in operation, rather than sole attention to one subcomponent.

In the following section, a rectifier and a buck-boost converter are introduced to the load impedance model of Figure 4(a) to examine the system-level behaviors and optimal DC power delivery conditions.

Analytical model formulation and solution for the nonlinear energy harvesting system with DC power management

System model and approximate solution to the governing equations

The governing equations of motion (equation (1)) are non-dimensionalized to be

$$x'' + \eta x' + (1-p)x + \beta x^3 + \kappa v_p = -z'' \quad (15a)$$

$$v_p' + i_p = \theta x' \quad (15b)$$

The non-dimensional base acceleration is

$$-z'' = a\cos\omega\tau \quad (16)$$

where a is the normalized base excitation of $\underline{a}$. Additional non-dimensional parameters are defined

$$\theta = \alpha x_0/(C_P V_0), \quad a = \frac{am}{k_1 x_0}, \quad I_p = \underline{I}_p/(C_P V_0 \omega_0), \quad V_p = \frac{V_p}{V_0} \quad (17)$$

The capital terms I_p, $\underline{I}_p$, V_p, and $\underline{V}_p$ are the amplitudes of the corresponding variables i_p, $\underline{i}_p$, v_p, and $\underline{v}_p$.

Assuming that the nonlinear energy harvester responds with oscillatory displacements with the same frequency as the base acceleration, the non-dimensional displacement is given by

$$x(\tau) = k(\tau) + h(\tau)\sin(\omega\tau) + g(\tau)\cos(\omega\tau) \quad (18)$$

Prior to having means to approximately solve for the system response, the characteristics of the non-dimensional voltage v_p and current i must be identified.

Figure 5 presents the interface circuit to which the nonlinear piezoelectric cantilever is attached. The circuit includes a rectifying bridge, smoothing capacitor C_1, and a buck-boost converter. The components in the green dashed box constitute the buck-boost converter
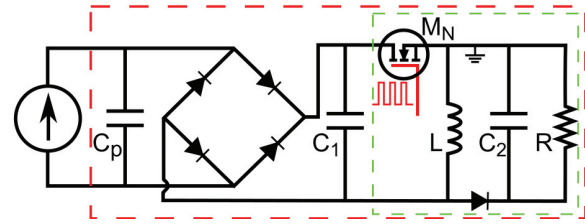
Figure 5. The nonlinear vibration energy harvester with a buck-boost converter.

that modulates the voltage across the load R so as to permit practical implementation of the DC power. Such power management is required because piezoelectric energy harvesters may generate high rectified voltages (>20 V), whereas many rechargeable batteries or microelectronics use low, standardized voltage levels such as 3 and 9 V. The inductor, capacitor, resistor, and diode in the buck-boost converter are labeled L, C_2, R, and D, respectively. The n-type metal-oxide-semiconductor field-effect transistor (MOSFET) M_N in the converter acts like a switch. A pulse width modulation (PWM) signal in red is sent to the gate of the MOSFET to control the open state.

In general, a buck-boost converter may run in two modes: DCM and continuous current mode (CCM). Compared to CCM, the switching losses are much less for DCM (Szarka et al., 2012), so that attention in this research is solely on the DCM operation. A buck-boost converter running in DCM will realize an impedance analogous to an equivalent resistance (Lefeuvre et al., 2007)

$$R_{eq} = \frac{2Lf_s}{D^2} \quad (19)$$

where L represents the inductance in the circuit; the switching frequency f_s and the duty cycle D are properties of the PWM signal. Since the behavior of the converter is not influenced by the real load R in Figure 5, the optimal working condition for a buck-boost converter will not change for different loads R. Therefore, the DCM operation is the preferred choice for energy harvesting applications.

Since the buck-boost converter in DCM can be replaced by an equivalent resistance R_{eq} (equation (19)), the interface circuit is reduced to a rectifier and an $R_{eq}C_1$ circuit. Based on previous studies (Dai and Harne, 2017; Liang and Liao, 2012), the non-dimensional voltage v_p across the piezoelectric beam capacitance C_p is

$$v_p = \left[\frac{-g(\tau)}{\pi}\theta\sin^2\Theta + \frac{h(\tau)}{2\pi}(2\Theta - \sin 2\Theta)\right]\sin\omega\tau$$

$$+ \left[\frac{h(\tau)}{\pi}\theta\sin^2\Theta + \frac{g(\tau)\theta}{2\pi}(2\Theta - \sin 2\Theta)\right]\cos\omega\tau \quad (20)$$

In equation (20), only the fundamental harmonic of voltage is considered on the basis that the fundamental contributes a significant proportion of the Fourier series reconstruction of the actual voltage signal (Dai and Harne, 2017; Liang and Liao, 2012). The parameters in equation (20) are

$$\Theta = \arccos\left(\frac{\pi\rho - 2\omega}{\pi\rho + 2\omega}\right), \quad \rho = \frac{1}{R_{eq}C_p\omega_0} \quad (21)$$

Then, equations (18) and (20) are substituted into equation (15a). Using the method of harmonic balance, equation (22) is then obtained. The roots of the polynomial (equation (22)) are the squared amplitudes of the non-dimensional displacement n^2. The voltage v_p is thereafter determined from equation (20)

$$(\Lambda_1^2 + X_1^2)n^2 = a^2 \quad (22)$$

The terms in equation (22) are

$$n^2 = g^2 + h^2, \quad \Lambda_1 = 1 - p + B\kappa - \omega^2 + \frac{3\beta n^2}{4} + 3\beta k^2,$$

$$X_1 = A\kappa + \eta\omega, \quad A = \frac{\theta\sin^2\Theta}{\pi}, \quad B = \frac{\theta(2\Theta - \sin 2\Theta)}{2\pi} \quad (23)$$

When a buck-boost converter operates in DCM, the voltage across the resistor R in Figure 5 is calculated by (Rogers, 1999)

$$\underline{V}_O = V_p V_0 D \sqrt{\frac{R}{2Lf_s}} \quad (24)$$

Then the DC output power is

$$\underline{P}_O = \frac{\underline{V}_O^2}{R} = \frac{V_p^2 V_0^2 D^2}{2Lf_s} \quad (25)$$

where V_p is the amplitude of v_p, $\underline{V}_O$ is the DC voltage across the resistor R, and $\underline{P}_O$ is the corresponding DC output power.

Determination of load impedance

The components in Figure 5 in the red dash-dot box are taken to be the load impedance $\underline{Z}_L$ for the nonlinear energy harvesting system. v_p is defined by equation (20). By equation (15b), the non-dimensional current that flows into the load is

$$i = \theta x' = \omega\theta[h\cos(\omega\tau) - g\sin(\omega\tau)] \quad (26)$$

In the following calculation, current and voltage are expressed in the complex exponential form for load impedance calculation

Table 2. Circuit components used for rectifier and buck-boost converter.

Component	Value or part
Rectifier diodes	1N4148 ($V_{d1} = 1$ V; $R_{d1} = 100\,\Omega$)
Diode D	Schottky 1N5820G ($V_{d2} = 0.37$ V; $R_{d2} = 0.37\,\Omega$)
C_1 (C_2)	10 μF (470 μF)
L	1 mH ($R_L = 0.216\,\Omega$)
M_N	IRLZ44 N ($V_{ds} = 1.3$ V; $R_{ds} = 0.022\,\Omega$)
R	2 kΩ

$$Z_L = \frac{v_p}{i} = \frac{\sqrt{A^2 + B^2}\,e^{j(\varphi_i - \varphi_v)}}{\omega\theta} \quad (27)$$

The phase angles are

$$\tan\varphi_v = \frac{-gA + hB}{hA + gB}, \quad \tan\varphi_i = -\frac{g}{h} \quad (28)$$

The corresponding dimensioned load impedance is thus

$$\underline{Z}_L = \frac{V_0\theta}{\alpha x_0\omega_0}Z_L \quad (29)$$

which yields the load resistance R_L and load reactance X_L

$$R_L = \frac{V_0 A}{\alpha x_0\omega_0\omega}, \quad X_L = \frac{-V_0 B}{\alpha x_0\omega_0\omega} \quad (30)$$

Validation of the analytical model formulation and solution

Power management circuit design

The specific circuit components used for electrical power management are listed in Table 2. In the experimental validation, the PWM signal is provided by a function generator (Siglent SDG 1025) instead of a self-powered oscillator (Kong et al., 2010). This approach to PWM signal generation inhibits the complication of the assessment of the principles studied here regarding the analytical prediction of optimal DC power delivery conditions. Future work will consider the methods of self-powering the power management circuit.

Experimental validation and comparison to the analytical and numerical results

The experimental system is used to validate the proposed analytical formulation for DC power optimization. In addition, verification of the accuracy of the approximate analytical solution is made by direct

consideration of the equations of motion via a MATLAB/Simulink model of the equivalent circuit, as shown in Figure 4(a), where $\underline{Z}_s$ is given by equation (12) and $\underline{Z}_L$ is given by equation (29). Runge–Kutta numerical integration is employed for any given base acceleration combination of amplitude and frequency. For such combination, eight randomly distributed sets of initial conditions are prescribed for the currents in order to ensure that the simulations identify all possible steady states of response in the nonlinear harvester structure and circuit system. The calculation time for each harmonic excitation condition is over 200 periods to ensure that the steady state is reached. The needs to utilize such long simulation times and multiple initial conditions make the simulation significantly more costly to compute than the analysis.

In order to take the losses of the electrical components into account, the respective forward voltage drops and the respective on-resistances for diodes and the MOSFET are employed in the analytical model and Simulink model. The values for the parameters are given in Table 2.

In the analysis, the output voltage with electrical losses can be written as (Rogers, 1999)

$$\underline{V}_O = \frac{V_{p1}V_0 D}{D_2} - V_{d2} - \underline{i}_L R_L - \frac{D}{D_2}\underline{i}_L(R_L + R_{ds}) \quad (31)$$

where D_2 relates to the time that the current through the inductor drops to zero; V_{d2} is the voltage drop of the diode; R_L and R_{ds} are the on-resistances of the inductor and MOSFET, respectively; $\underline{i}_L$ is the current through the inductor; and V_{p1} is the input voltage of the buck-boost converter, which is the voltage across the capacitor C_1. Considering the losses caused by the rectifier bridge, V_{p1} can be expressed as

$$V_{p1} = V_p - 2V_{d1} - 2\underline{i}_p R_{d1} \quad (32)$$

where V_{d1} and R_{d1} are the voltage drop and on-resistance of the diode in the rectifier bridge, respectively.

Since the currents $\underline{i}_L$, $\underline{i}_p$ and the on-resistances R_L, R_{ds} are relatively small values, equations (31) and (32) are approximated by

$$\underline{V}_O = \frac{V_{p1}V_0 D}{D_2} - V_{d2} \quad (33)$$

$$V_{p1} = V_p - 2V_{d1} \quad (34)$$

The expression for D_2 adopted is

$$D_2 = \sqrt{\frac{2Lf_s}{R}} \quad (35)$$

Figure 6(a) presents the amplitude of the harvester displacement determined by analysis and simulation. The base acceleration amplitude is 9.8 m/s^2 and the

excitation frequency is around the linearized natural frequency of 30 Hz. Since greater values of the buck-boost converter switching frequency result in greater losses, in this work the switching frequency remains at 1 kHz in all evaluations. As a result of the switching frequency selection, it is recognized that the preferred range of duty cycle may be less than 1% (Kong et al., 2010). For the specific result presented in Figure 6(a), the duty cycle is 0.1%. Based on the analytical and simulation results, the large-amplitude snap-through responses and small-amplitude intrawell responses coexist in the lower frequency range, such around 10–17 Hz. In the frequency range around 20 Hz, only snap-through responses occur. The simulation predicts a narrower range of frequencies across which only snap-through exists compared to analysis (Harne and Wang, 2017). At higher frequencies such as 30 Hz, both simulation and analysis agree that an intrawell response alone may occur. In the range from 23 to 30 Hz, the simulations yield aperiodic oscillations that result in different amplitudes of displacement based on the initial conditions of the simulation. In contrast, the analysis, based on the method of harmonic balance and steady-state assumptions, predicts that either an intrawell or a snap-through behavior may occur. These trends are seen elsewhere in the literature that compares analytical predictions to numerical simulations of nonlinear dynamics of vibration energy harvesters around frequency bands of coexistent responses (Dai and Harne, 2017; Panyam et al., 2014).

Figure 6(b) shows the corresponding experimental results. Compared to the model results, the large-amplitude snap-through dynamic occurs only in the frequency band from 20 to 25 Hz and the displacement amplitude of intrawell oscillations at higher frequencies is larger. One explanation for this discrepancy is a minor imperfection between the two stable equilibria. Asymmetry of stable equilibria is known to result in displacement amplitudes among the dynamic steady states that are nearer in value than in the case of perfect symmetry (Goodpaster and Harne, 2018; Kovacic et al., 2008). In addition, the piezoelectric cantilever contains layers of FR4 glass–reinforced epoxy laminate substrate, piezoelectric PZT-5H, and copper electrodes. The FR4 layers may possess viscoelastic, and thus time-dependent, material properties that cause more intricate damping influences than the viscous damping model currently employed in the model formulation. These details of experimental system design and implementation may be introduced in a refined model formulation in future investigations. Yet, despite such deviation associated with inevitable limitations to achieve perfect configurations in experiments, the experimental results are in good qualitative and quantitative agreement with the analytical and simulation results, giving validation support to the model formulation and solution efforts.
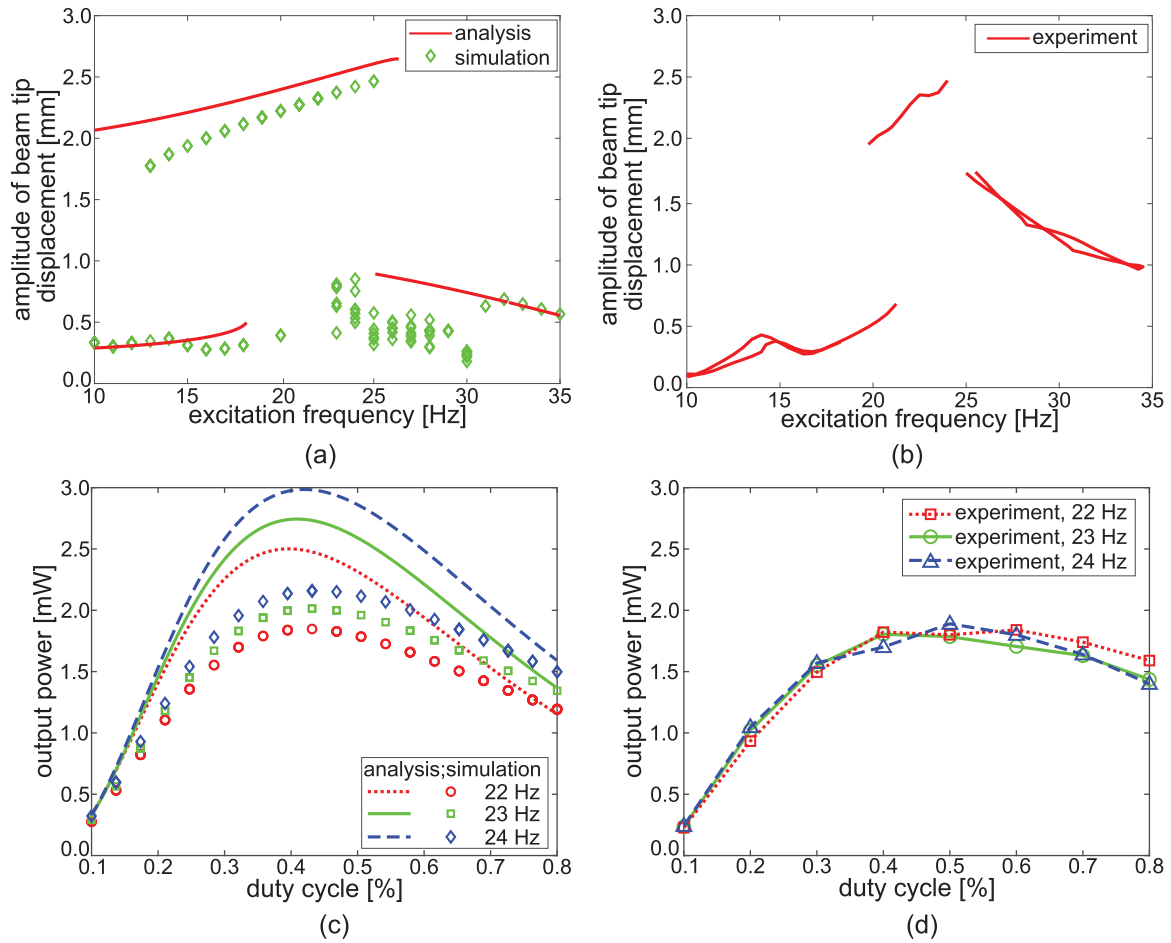
Figure 6. Mechanical and electrical responses of (a) beam tip displacement amplitude predicted by analysis and simulation and (c) output power at different excitation frequencies given by analysis and simulation; (b) and (d) the corresponding results from experiments.

Snap-through behavior is predicted by the modeling and experiment in the frequency range from 21 to 24 Hz. To validate the model predictions of the DC power delivery from the buck-boost converter, the frequencies of 22, 23, and 24 Hz are considered. The output power shown in Figure 6(c) and (d) corresponds to the power delivered to the load R. The analysis in Figure 6(c) predicts the greatest DC power delivery among all the results. Because the analysis idealizes the response in steady state as being from a single harmonic, no higher order losses are incurred in the analytical prediction that otherwise occur for the simulation and experiment. In addition, both the simulation and the experimental system are influenced by much more detailed losses of the electrical components, like the on-resistances of the diodes and MOSFET that contribute to smaller output powers in the simulation and experiment shown in Figure 6(c) and (d), respectively. Despite this discrepancy, all three methods of assessment identify the same strategy for optimization using the nonlinear energy harvester with buck-boost converter. Specifically, the optimal duty cycles at the three

frequencies are all around 0.4%–0.5%. In addition, a greater reduction of the DC power occurs for duty cycles less than this optimal range than above this range, which is manifest in all of the results.

Overall, the good qualitative and quantitative agreement among all the analytical, simulation, and experimental results establishes the efficacy of the analytical model formulation to characterize the mechanical and electrical behavior of the nonlinear energy harvesting system.

An impedance-based assessment for optimal DC power delivery

After validating the analytical method, the same parameters shown in Table 2 are considered to conduct a thorough analysis to reveal the relationships between impedance change and optimal output power. For the proposed harvesting system, the structural dynamics $x(\tau)$ and electrical voltage across the piezoelectric beam $v_p(\tau)$ are obtained by solving the cubic polynomial equation (22). The corresponding output power $\underline{P_O}$ is

then determined by equation (25). Figure 7 shows the output power across the load R at different base acceleration frequencies and buck-boost converter duty cycles. The white dashed line displays the duty cycle at each frequency to deliver the maximum DC power. A clear frequency dependence of the duty cycle to maximize the DC power is observed in the analytical results shown in Figure 7.

With equations (12) and (29), the source and load impedances are, respectively, obtained. Figure 8 presents the corresponding impedance results using the same x and v_p values that are computed for the results shown in Figure 7. Figure 8(a) and (b) shows the influence of change in excitation frequency and duty cycle on the source resistance and reactance, respectively. The source resistance R_s in Figure 8(b) is constant at 99 kΩ, as described in section "Source impedance characterization." The absolute value of the source reactance X_s decreases with increase in the excitation frequency and increases with increase in the duty cycle (Figure 8(a)). When the source reactance is zero, snap-through behavior is no longer possible. Figure 8(c) and (d) presents the load impedance results. Although
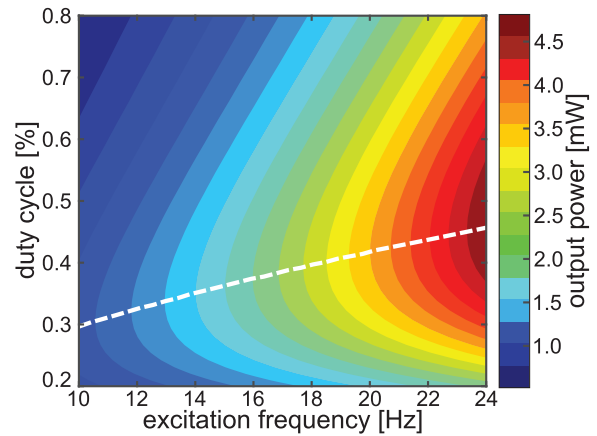

Figure 7. Analytical prediction of DC power delivery at the base acceleration amplitude of 9.8 m/s² considering the entire nonlinear energy harvester and power management circuit. The white dashed line shows the duty cycle at each frequency to generate the maximum DC power.

the buck-boost converter displays a pure resistance property, combined with the rectifier bridge and
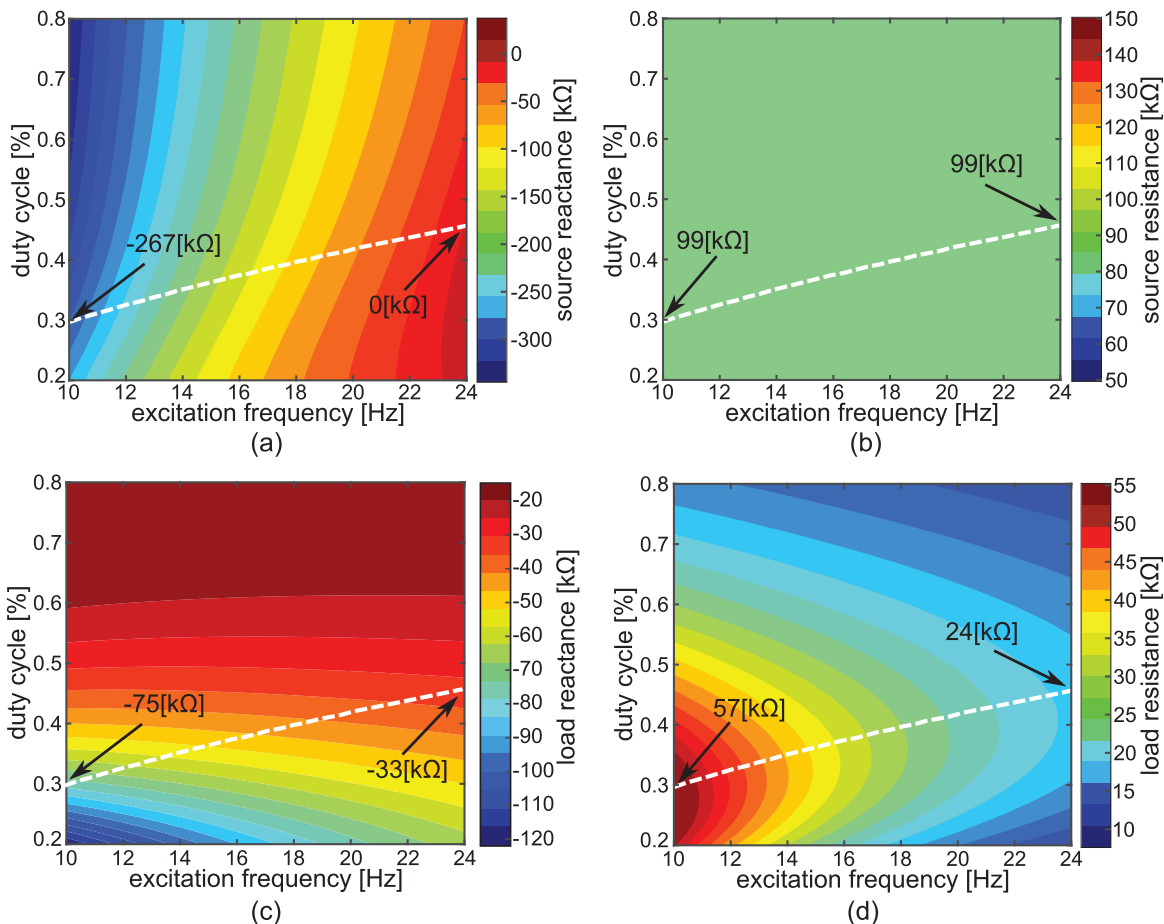
Figure 8. Impedance results at the base acceleration amplitude of 9.8 m/s² of (a) source reactance and (b) source resistance and (c) load reactance and (d) load resistance.
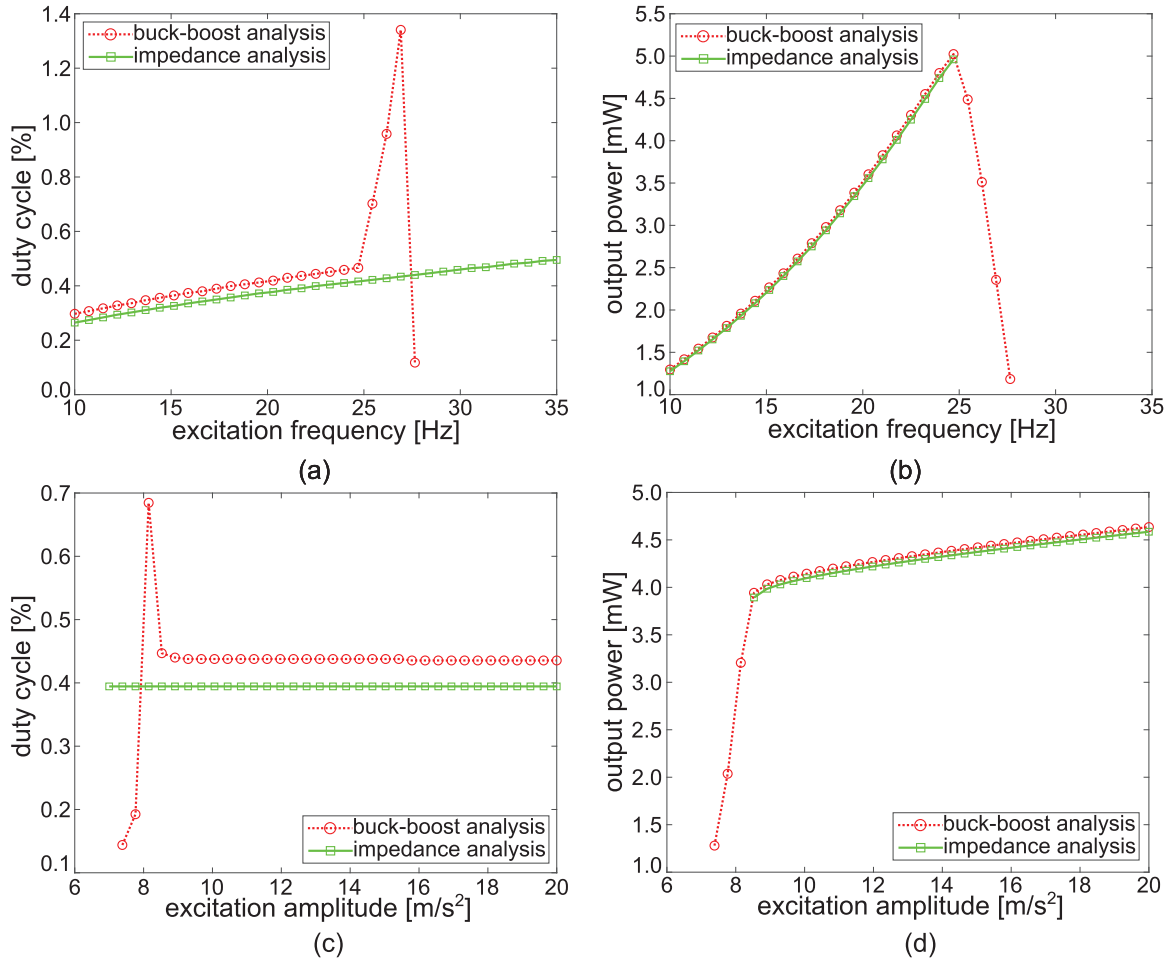
Figure 9. (a) Optimal duty cycle of the nonlinear energy harvesting system at different excitation frequencies with a base acceleration amplitude of 9.8 m/s^2; (b) the optimal output power corresponding to (a); (c) optimal duty cycle at different base acceleration amplitudes with an excitation frequency of 22 Hz; (d) the optimal output power corresponding to (c).

piezoelectric capacitance, the load reactance X_L is influenced by duty cycle and base acceleration frequency. In addition, from Figure 8(d), the load resistance R_L presents a maximum value with changing duty cycle at each frequency.

Based on conservation of energy, the power delivered to the load R in Figure 5 is equal to the power across $\underline{Z}_L$ in Figure 4(a). Consequently, this output power is

$$\underline{P}_o = \frac{V_s^2 R_L}{(R_S + R_L)^2 + (X_s + X_L)^2} \quad (36)$$

By conventional impedance matching theory, the optimal output power is delivered when the load impedance is the complex conjugate of the source impedance, in other words, when $R_L = R_S$ and $X_L = -X_S$. Yet, in the case of this study, the source reactance varies based on the base acceleration frequency and the buck-boost converter duty cycle, as shown in Figure 8(a). In addition, the load resistance and reactance are

unable to realize the same reactance and resistance values as a conjugate of the source impedance. This is observed by comparing Figure 8(c) to (a) and Figure 8(d) to (b) wherein it is found that the load reactance in Figure 8(c) takes on the same sign as the source reactance in Figure 8(a). Also, the maximum load resistance in Figure 8(d) is less than the source resistance in Figure 8(b). In other words, the conventional impedance matching theory is not able to be employed.

Yet, despite this limitation, the results of Figure 8 indicate that a suboptimal set of working conditions in the duty cycle and base acceleration frequency are identified that still yield peak output power. The white dashed lines in Figure 8 correspond to the full system analysis from Figure 7 that results in the optimal working conditions. For Figure 8(d), the white dashed line follows the peak value of resistance for the given duty cycle and excitation frequency. Although this value still falls short of the source resistance 99 kΩ, the load resistance is maximized and thus nearest to the ideal condition.

Because the phase of the load impedance is influenced by an intricate combination of power management circuit characteristics (see equations (21), (23), and (30)), the load reactance and resistance are unable to be individually selected for the sake of maximizing output power. Based on equation (36), the influences of load resistance and reactance on the output power are expressed in equation (37). Here the sum of source and load reactance is taken as a new variable $K = X_S + X_L$

$$
\begin{aligned}
\frac{\partial \underline{P}_o}{\partial R_L} &= \underline{V}_s^2 \cdot \frac{(X_s + X_L)^2 - R_L^2 + R_S^2}{\left[(R_S + R_L)^2 + (X_s + X_L)^2\right]^2} \\
&= \underline{V}_s^2 \cdot \frac{K^2 - R_L^2 + R_S^2}{\left[(R_S + R_L)^2 + K^2\right]^2}
\end{aligned}
\quad (37a)
$$

$$
\begin{aligned}
\frac{\partial \underline{P}_o}{\partial K} &= \underline{V}_s^2 \cdot \frac{-2(X_s + X_L)R_L}{\left[(R_S + R_L)^2 + (X_s + X_L)^2\right]^2} \\
&= \underline{V}_s^2 \cdot \frac{-2K R_L}{\left[(R_S + R_L)^2 + K^2\right]^2}
\end{aligned}
\quad (37b)
$$

By setting equations (37a) and (37b) to zero and solving for R_L and K, the impedance matching condition is obtained. Considering the parameters of the energy harvesting platform studied here, the comparison of load and source resistance reveals

$$R_S > 2R_L \quad (38)$$

Therefore, the absolute difference of the two gradients is

$$
\left|\frac{\partial P_o}{\partial R_L}\right| - \left|\frac{\partial P_o}{\partial K}\right| > \underline{V}_s^2 \cdot \frac{K^2 + R_L^2 - 2|K|R_L}{\left[(R_S + R_L)^2 + K^2\right]^2} > 0 \quad (39)
$$

Equation (39) reveals that the change in output power caused by resistance change is more influential than the change in output power that results from the change in reactance. Specifically, when $R_S > 2R_L$ the resistance becomes a more influential factor toward the optimal conditions of duty cycle at different base excitation conditions for greater peak output power. This result explains the fact that the load resistance maxima in Figure 8(d) correlate to the peak DC power operating conditions computed from the full analysis (see the white dashed curve in Figure 8(d) that is obtained from the maxima in Figure 7).

Optimal duty cycle predicted by impedance analysis

From the analysis of the previous section, although the conventional approach to impedance matching is not possible using the nonlinear energy harvesting system considered here, a suboptimal matching condition still maximizes the output power. To investigate this suboptimal approach to optimization in further detail, the insight that resistance matching is more influential in the output power is studied further. Equation (36) is taken omitting the influence of reactance

$$\underline{P} = \frac{\underline{V}_s^2 R_L}{(R_L + R_s)^2} \quad (40)$$

The equivalent voltage $\underline{V}_s$ and source resistance R_s are constants. In other words, the only variable in equation (40) is R_L, which is related to circuit parameters according to equation (30).

The red dotted curves with circular data points in Figure 9 represent the results from the analysis considering both the harvester structure and buck-boost converter, termed the "buck-boost analysis." The results from the buck-boost analysis are derived from the procedures described in section "System model and approximate solution to the governing equations." To obtain the results shown in Figure 9, using the buck-boost analysis, equation (22) is solved to identify base acceleration excitation frequency, excitation amplitude, and the duty cycle that lead to optimal working conditions. The green solid curves with square data points in Figure 9 correspond to the "impedance analysis" that is computed using equations (21), (23), (30), and (40). From 10 Hz, for an increase in the excitation frequency, the optimal duty cycle slightly increases from around 0.3% to 0.5% according to the impedance analysis. Yet, for an increase in the excitation frequency around 25 Hz, an abrupt increase in optimal duty cycle is observed in the buck-boost analysis. This large qualitative change in the optimal working conditions of the converter is due to the loss of snap-through dynamics, shown in Figure 10. Figure 10(a) and (b) presents the amplitude of displacement and the resulting output power for the base acceleration frequencies of 22, 26, and 27.3 Hz when the base acceleration amplitude is 9.8 m/s^2, respectively. As the frequency increases, the responses separate into two branches. As observed in Figure 10(b), the peak power condition therefore shifts to conditions of higher duty cycle. This trend disagrees with the impedance matching–based results in Figure 9(a) that presumes the snap-through behavior may persist for all frequencies. Yet, despite this nuance of prediction capability, the output DC powers predicted by the buck-boost and impedance analyses are in good quantitative agreement verifying the viability of the impedance matching–based analysis to characterize the primary trends.

A similar analysis is conducted by studying the role of change in the base acceleration amplitude in Figure 9(c) and (d). For amplitudes of the base acceleration from 7 to 9 m/s^2, the snap-through dynamic is not possible for all duty cycles for the 22 Hz frequency. This
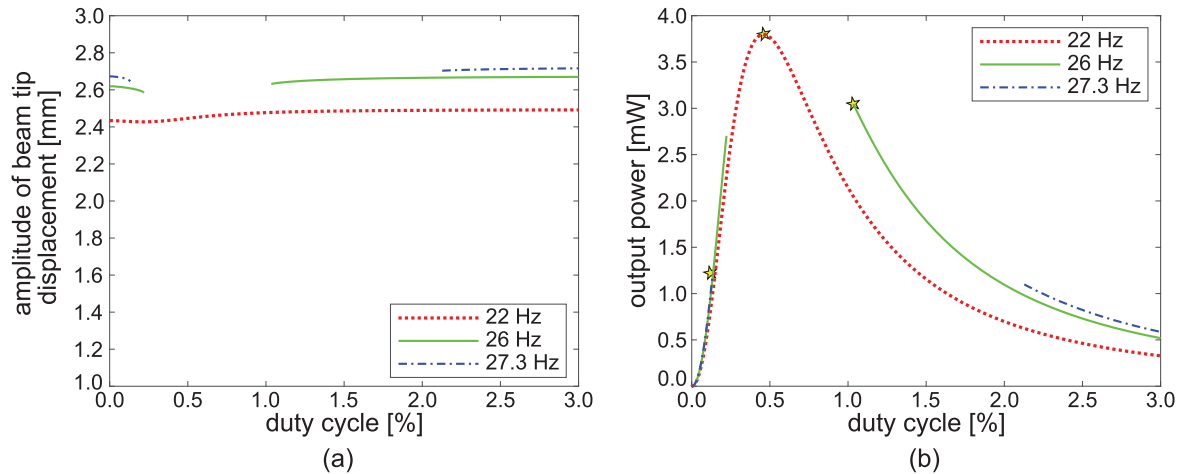
Figure 10. (a) Amplitude of beam tip displacement at a base acceleration amplitude of 9.8 m/s^2 and (b) the corresponding output power as a function of duty cycle at a base acceleration amplitude of 9.8 m/s^2.

explains the sudden variation in the buck-boost analysis optimal duty cycle that is not evident by the impedance analysis. For base acceleration amplitude greater than 9 m/s^2, the optimal duty cycle changes slightly in both analytical approaches. On the other hand, since the base acceleration amplitude does not affect the load resistance, the change of load resistance is the same at each of the base acceleration amplitude, which explains the constant optimal duty cycle determined by the impedance analysis. These results establish confidence in the source impedance analysis.

Based on the results shown in Figure 9, the optimal working condition for the nonlinear vibration energy harvester interfaced with a buck-boost converter may be determined by the impedance analysis. In contrast to the buck-boost analysis itself, the impedance analysis only requires information regarding the source and load resistances. Since both resistances are derived in sections "Source/load modeling of nonlinear energy harvesting system" and "Analytical model formulation and solution for the nonlinear energy harvesting system with DC power management," this research identifies an efficient means by which to evaluate the optimal working condition of the energy harvesting system.

Conclusion

This research exploits the perspective of impedance to examine the optimal DC power operation of a nonlinear energy harvester interfaced with a buck-boost converter for practical electrical power management. The internal, or source, impedance of the nonlinear harvester platform is shown to be influenced by change in the driven conditions of frequency and amplitude. Because such changes challenge the conventional impedance matching concepts, a rigorous analytical study is undertaken to

uncover means to maximize DC power delivery from the system despite the inability to obtain conventional complex conjugate impedance matching. After validating the analysis, the output power results and impedance results are shown to demonstrate a suboptimal condition for maximum DC power delivery through the buck-boost converter. By studying the suboptimal conditions in detail, it is explicitly revealed that resistance of the load plays a more influential role for the system optimization. With this insight, a simplified method of DC power maximization is created that considers only the load and source resistances to optimize the working conditions. Both the predicted duty cycle and output power from such reduced modeling strategy show good agreement with the whole system analysis, exemplifying the strength of the analytical formulation established here upon impedance principles.

Declaration of conflicting interests

The author(s) declared no potential conflicts of interest with respect to the research, authorship, and/or publication of this article.

ORCID iD

Ryan L Harne https://orcid.org/0000-0003-3124-9258

References

Beeby SP, Tudor MJ and White NM (2006) Energy harvesting vibration sources for microsystems applications. *Measurement Science and Technology* 17: R175–R195.

Chandrakasan A, Amirtharajah R, Goodman J, et al. (1998) Trends in low power digital signal processing. *Proceedings of the 1998 IEEE International Symposium on Circuits and Systems* 4: 604–607.

Cottone F, Vocca H and Gammaitoni L (2009) Nonlinear energy harvesting. *Physical Review Letters* 102: 080601.

Dai Q and Harne RL (2017) Investigation of direct current power delivery from nonlinear vibration energy harvesters under combined harmonic and stochastic excitations. *Journal of Intelligent Material Systems and Structures* 29: 514–529.

Davis WR, Zhang N, Camera K, et al. (2002) A design environment for high-throughput low power dedicated signal processing systems. *IEEE Journal of Solid-State Circuits* 37: 420–431.

Erturk A and Inman DJ (2008) A distributed parameter electromechanical model for cantilevered piezoelectric energy harvesters. *Journal of Vibration and Acoustics* 130: 041002.

Erturk A and Inman DJ (2011) Broadband piezoelectric power generation on high-energy orbits of the bistable duffing oscillator with electromechanical coupling. *Journal of Sound and Vibration* 330: 2339–2353.

Erturk A and Inman DJ (2011) *Piezoelectric Energy Harvesting*. Chichester: John Wiley & Sons.

Erturk A, Hoffmann J and Inman DJ (2009) A piezomagnetoelastic structure for broadband vibration energy harvesting. *Applied Physics Letters* 94: 254102.

Feeny BF, Yuan CM and Cusumano JP (2001) Parametric identification of an experimental magneto-elastic oscillator. *Journal of Sound and Vibration* 247: 785–806.

Ferrari M, Ferrari V, Guizzetti M, et al. (2010) Improved energy harvesting from wideband vibrations by nonlinear piezoelectric converters. *Sensors and Actuators A: Physical* 162: 425–431.

Garbuio L, Lallart M, Guyomar D, et al. (2009) Mechanical energy harvester with ultralow threshold rectification based on SSHI nonlinear technique. *IEEE Transactions on Industrial Electronics* 56: 1048–1056.

Goodpaster BA and Harne RL (2018) Analytical modeling and impedance characterization of the nonlinear dynamics of thermomechanically coupled structures. *Journal of Applied Mechanics* 85: 081010.

Gu L and Livermore C (2011) Impact-driven, frequency up-converting coupled vibration energy harvesting device for low frequency operation. *Smart Materials and Structures* 20: 045004.

Guyomar D, Badel A and Lefeuvre E (2005) Toward energy harvesting using active materials and conversion improvement by nonlinear processing. *IEEE Transactions on Ultrasonics, Ferroelectrics, and Frequency Control* 52: 584–595.

Harne RL and Wang KW (2013) A review of the recent research on vibration energy harvesting via bistable system. *Smart Materials and Structures* 22: 023001.

Harne RL and Wang KW (2017) *Harnessing Bistable Structural Dynamics: For Vibration Control, Energy Harvesting and Sensing*. Chichester: John Wiley & Sons.

Harne RL, Thota M and Wang KW (2013) Bistable energy harvesting enhancement with an auxiliary linear oscillator. *Smart Materials and Structures* 22: 125028.

Hikihara T and Kawagoshi T (1996) An experimental study on stabilization of unstable periodic motion in magneto-elastic chaos. *Physics Letters A* 211(1): 29–36.

Jawad HW, Nordin R, Gharghan SK, et al. (2017) Energy-efficient wireless sensor networks for precision agriculture: a review. *Sensors* 17: E1781.

Kong N, Ha DS, Erturk A, et al. (2010) Resistive impedance matching circuit for piezoelectric energy harvesting. *Journal of Intelligent Material Systems and Structures* 21: 1293–1302.

Kovacic I, Brennan MJ and Lineton B (2008) On the resonance response of an asymmetric duffing oscillator. *International Journal of Non-linear Mechanics* 43: 858–867.

Lam YH, Ki WH and Tsui CY (2006) Integrated low-loss CMOS active rectifier for wirelessly powered devices. *IEEE Transactions on Circuits and Systems II: Express Briefs* 53(12): 1378–1382.

Le TT, Han J, von Jouanne AV, et al. (2006) Piezoelectric micro-power generation interface circuits. *IEEE Journal of Solid-State Circuits* 41(6): 1411–1420.

Lefeuvre E, Audigier D, Richard C, et al. (2007) Buck-boost converter for sensorless power optimization of piezoelectric energy harvester. *IEEE Transactions on Power Electronics* 22(5): 2018–2025.

Lefeuvre E, Badel A, Richard C, et al. (2006) A comparison between several vibration-powered piezoelectric generators for standalone systems. *Sensors and Actuators A: Physical* 126(2): 405–416.

Liang J and Liao WH (2012) Impedance modeling and analysis for piezoelectric energy harvesting systems. *IEEE/ASME Transactions on Mechatronics* 17(6): 1145–1157.

Makihara K, Onoda J and Miyakawa T (2006) Low energy dissipation electric circuit for energy harvesting. *Smart Materials and Structures* 15: 1493–1498.

Mitcheson PD, Yeatman EM, Rao GK, et al. (2008) Energy harvesting from human and machine motion for wireless electronic devices. *Proceedings of the IEEE* 96: 1457–1486.

Moon FC and Holmes PJ (1979) A magnetoelastic strange attractor. *Journal of Sound and Vibration* 65(2): 275–296.

Ottman GK, Hofmann HF, Bhatt AC, et al. (2002) Adaptive piezoelectric energy harvesting circuit for wireless remote power supply. *IEEE Transactions on Power Electronics* 17: 669–676.

Panyam M, Masana R and Daqaq MF (2014) On approximating the effective bandwidth of bi-stable energy harvesters. *International Journal of Non-linear Mechanics* 67: 153–163.

Rogers E (1999) *Understanding buck-boost power stages in switch mode power supplies*. Application Report SLVA057. Texas Instruments. Available at: http://www.ti.com/lit/an/slva059a/slva059a.pdf

Roundy S and Zhang Y (2005) Toward self-tuning adaptive vibration based micro-generators. *Smart Structures, Devices, and Systems II* 5649: 373–385.

Scarselli G, Nicassio F, Pinto F, et al. (2016) A novel bistable energy harvesting concept. *Smart Materials and Structures* 25: 055001.

Sebald G, Kuwano H, Guyomar D, et al. (2011) Experimental duffing oscillator for broadband piezoelectric energy harvesting. *Smart Materials and Structures* 20: 102001.

Shafer MW, MacCurdy R, Shipley JR, et al. (2015) The case for energy harvesting on wildlife in flight. *Smart Materials and Structures* 24: 025031.

Szarka GD, Stark BH and Burrow SG (2012) Review of power conditioning for kinetic energy harvesting systems. *IEEE Transactions on Power Electronics* 27(2): 803–815.

Wu Y, Badel A, Formosa F, et al. (2014) Nonlinear vibration energy harvesting device integrating mechanical stoppers used as synchronous mechanical switches. *Journal of Intelligent Material Systems and Structures* 25: 1658–1663.

Xiao Z, Yang TQ, Dong Y, et al. (2014) Energy harvester array using piezoelectric circular diaphragm for broadband vibration. *Applied Physics Letters* 104: 223904.

Yang Y and Tang L (2009) Equivalent circuit modeling of piezoelectric energy harvesters. *Journal of Intelligent Material Systems and Structures* 20: 2223–2235.